A Diabatic Lagrangian Technique for the Analysis of Convective Storms. Part II: Application to a Radar-Observed Storm

CONRAD L. ZIEGLER

NOAA/National Severe Storms Laboratory, Norman, Oklahoma

(Manuscript received 21 February 2013, in final form 24 May 2013)

ABSTRACT

A new diabatic Lagrangian analysis (DLA) technique that derives predicted fields of potential temperature, water vapor and cloud water mixing ratios, and virtual buoyancy from three-dimensional, time-dependent wind and reflectivity fields (see Part I) is applied to the radar-observed 9 June 2009 supercell storm during the Second Verification of the Origins of Rotation in Tornadoes Experiment (VORTEX2). The DLA diagnoses fields of rain and graupel content from radar reflectivity and predicts the evolution of analysis variables following radar-inferred air trajectories in the evolving storm with application of the diagnosed precipitation fields to calculate Lagrangian-frame microphysical processes. Simple damping and surface flux terms and initialization of trajectories from heterogeneous, parametric mesoscale analysis fields are also included in the predictive Lagrangian calculations. The DLA output compares favorably with observations of surface in situ temperature and water vapor mixing ratio and accumulated rainfall from a catchment rain gauge in the 9 June 2009 storm.

1. Introduction

The retrieval of the evolving 3D buoyancy field in convective storms with multiple-Doppler radar observations is potentially helpful in deducing the dynamical forcing of airflow in observed supercell storms (e.g., Klemp 1987). In combination with the 3D buoyancy field estimated from microphysical continuity retrieval (e.g., Ziegler 1985) or other methods, the 3D perturbation pressure field may be recovered via dynamic retrieval (e.g., Brandes 1984) to investigate airflow dynamics. However, hybrid retrievals that combine buoyancy and water substance retrievals with dynamically retrieved quantities may provide a more robust combination of pressure and buoyancy fields than may be obtained via conventional pressure–buoyancy retrievals (e.g., Hauser and Amayenc 1986; Hane et al. 1988). Knowledge of the observed buoyancy field as it relates to the development of low-level rotation in supercell storms (e.g., Rotunno and Klemp 1985) is an important research objective of the recent second Verification of the Origins of Rotation in Tornadoes Experiment (VORTEX2, 2009–10; Wurman et al. 2012). This paper demonstrates the application of a new buoyancy retrieval method, termed diabatic Lagrangian analysis (DLA), to a radar-observed supercell storm.

Part I (Ziegler 2013, hereafter Z13) described the DLA algorithm and demonstrated it via an Observing System Simulation Experiment (OSSE), wherein the DLA's input wind and reflectivity fields were provided from a simulated storm. However, the implications of potential differences between radar-observed and modeled winds and reflectivities should be considered via the application of DLA to observed storms. For example, radar observation and analysis may introduce varying amounts of error into the derived wind velocity owing to such factors as absence of radial velocity observations below the base-elevation scan (discussed further in sections 2d and 3d), beam averaging of radial velocity (Doviak and Zrnic 1984; Wood and Brown 1997), the local multiple-radar observing geometry (Ray and Sangren 1983), spatial filtering during single-radar objective analysis (e.g., Majcen et al. 2008), and error accumulation during vertical integration of the mass continuity equation (Ray et al. 1980b; Kessinger et al. 1987). Radar reflectivity measurements are also derived from potentially complex mixtures of varying habits, shapes, and

Corresponding author address: Dr. Conrad L. Ziegler, National Severe Storms Laboratory, Forecast Research and Development Division, 120 David L. Boren Blvd., Norman, OK 73072.
E-mail: conrad.ziegler@noaa.gov

DOI: 10.1175/JTECH-D-13-00036.1

sizes of liquid and ice hydrometeors, whereas model reflectivity is computed from a reduced set of simulated parameterized precipitation distributions using highly simplified backscatter models. Hence, although the DLA method successfully reproduced the structure of a simulated supercell (Z13), it must be independently tested and evaluated in the case of a radar-observed storm in which in situ observations are available to validate derived buoyancies. Whereas model-output fields are internally consistent, the assimilation of the independent and morphologically more complex radar measurements and validation with in situ data in an observed storm collectively provide a more robust test of the DLA.

This paper demonstrates the performance of the DLA method in the radar-observed 9 June 2009 Greensburg, Kansas, supercell storm during VORTEX2, which developed a transient but strong low-level mesocyclone and also a short-lived, concentrated (possibly with tornadic intensity) vortex as inferred from mobile Doppler radar measurements. The DLA is validated by comparing its output with storm-scale surface in situ observations and gauge-measured hourly surface rainfall in the 9 June Greensburg storm.

2. Diabatic Lagrangian analysis of a radar-observed storm

a. Overview of the diabatic Lagrangian analysis algorithm

Although the DLA method was described in detail in Z13, its salient characteristics as applied to radar-observed storms are briefly recapitulated. The DLA predicts the 3D fields of potential temperature θ, water vapor mixing ratio q_v, and cloud water mixing ratio q_c by integrating a set of time-dependent ordinary differential equations (ODEs) for the predictive variables along air trajectories that terminate at the grid points of the analysis domain (i.e., one trajectory per grid point). The ODEs combine Lagrangian transport with rate terms describing the evolutions of θ, q_v, and q_c via parameterizations of selected warm- and cold-cloud microphysical processes and simplified representations of mixing effects and surface fluxes. To calculate microphysical processes at the individual Lagrangian points following the motion, the DLA combines the predicted Lagrangian values of θ, q_v, and q_c with diagnosed values of rain and graupel total concentrations and mixing ratios (i.e., N_r, N_g, q_r, and q_g, respectively) that are inferred from the time-spaced fields of radar-analyzed reflectivity Z_H (dBZ). Small high-density hail is implicitly included within the DLA's graupel category, while large hail content is not presently diagnosed.

The application of the DLA method to an observed storm involves calculating backward ground-relative air trajectories using time-spaced radar-analyzed fields of the west–east (u), south–north (v), and vertical (w) wind components in a fixed analysis domain. The DLA algorithm verifies that each backward gridpoint trajectory has terminated in the observed storm's environment via robust conditional tests (Z13). The Lagrangian values of θ, q_v, and base-state pressure p_B at the initial point and time for forward integration are interpolated from a simple 3D mesoscale analysis and the base-state sounding (as described in section 3b), while q_c is initialized to zero. The DLA is completed by gathering the 3D fields composed of the ending Lagrangian values from the set of all gridpoint trajectories, with hole-filling and application of a low-pass filter to suppress infrequent missing values (i.e., noninitialized trajectories) and any poorly resolved small-scale ($\sim$2–3Δ) variations between neighboring trajectories.

b. Single-radar objective analysis and multiple-Doppler wind synthesis

The Doppler radar data employed in the present study have been extensively edited using SOLOII software (Oye et al. 1995) to remove ground targets and weak or range-folded echoes, apply rotation corrections for mobile radar orientation relative to true north (Wurman and Gill 2000; Ziegler et al. 2004), and de-alias radial velocities. Spatial interpolation of edited radial velocity and reflectivity data to a regular Cartesian grid is managed with a multipass Barnes scheme (Majcen et al. 2008). The lowest grid level is located at the surface (necessitating a modest downward extrapolation from the elevation angle of the base radar sweep) to facilitate comparisons of radar winds and DLA output fields with surface in situ measurements. The single-radar analyses are optimized to obtain uniform smoothness over the entire analysis domain while minimizing the amplitude of unresolved scales. The filtering parameter $\kappa = (1.33\Delta)^2$ has been carefully chosen to adequately damp scales less than $\sim 3\Delta$ (Pauley and Wu 1990), where Δ is the coarsest mean gate spacing in either azimuth or elevation in the analyzed storm volume. The analysis employs a Barnes convergence parameter value of $\gamma = 0.3$. An optimal grid spacing δ ranges from $\Delta/4$ to $\Delta/2$.

The 3D vector airflow field is synthesized from the objectively analyzed multiradar radial velocities using an overdetermined analysis algorithm (Ray et al. 1980b; Ray and Sangren 1983; Kessinger et al. 1987). A system composed of two normal linear equations for the u, v, and w components that include local summations of radial velocities from all radars are solved iteratively during vertical integration of the anelastic mass continuity

equation to obtain the vector air velocity field [i.e., Eqs. (A2)–(A4) of Kessinger et al. 1987]. Vertical integration of mass continuity in the overdetermined system proceeds through a given level in each grid column if radial velocities are present from two or more radars. Two wind syntheses are produced by integrating the continuity equation upward from ground level and downward from storm top and assuming $w = 0$ at the initial levels (e.g., Ray et al. 1980b). A single synthesized wind analysis combining the two boundary conditions with the effects of the integrated divergences on the horizontal winds is obtained via a weighted average of the individual vector velocity analyses. The weight for the upward and downward integrations is a linear function that varies according to the fractional vertical grid distance at a given grid level between the surface and the height at which the upper boundary condition is applied in each grid column. The radar-synthesized velocity components at the edge of the wind analysis area at each level are blended with the horizontal winds $u_{\mathrm{env}}(z)$ and $v_{\mathrm{env}}(z)$ from an environmental sounding (i.e., assuming $w_{\mathrm{env}} = 0$) via repeated application of a horizontal nine-point elliptic low-pass spatial filter at any grid point where reflectivity is below 20 dBZ. The latter simple low-pass spatial filtering procedure generates a gradual, continuous transition of the local wind field from the radar-observed, unsmoothed storm's edge to the smoothed, sounding-weighted environment.

Variational analysis methods are available to exactly satisfy the anelastic mass continuity equation with upper and lower kinematic boundary conditions via either a strong integral constraint (e.g., Ray et al. 1980b; Ziegler et al. 1983) or a strong local constraint (Ray et al. 1978). However, the above analysis obtained by averaging the upward and downward integrations is expected to produce very similar results to analysis E of Ray et al. (1980b), which combined a direct least squares horizontal wind field estimate with a variational integral constraint. Therefore, the available variational velocity adjustment techniques have not been applied in the present study. An inequality constraint adjustment has been applied to check that the vertical velocity does not exceed a fraction F_w of the maximum parcel theory updraft magnitude W_{PT} (here, F_w is ~0.8). The inequality constraint is imposed by subtracting a height-dependent fraction of W_{PT} from the local unadjusted w value, with the fraction decreasing from 100% at the equilibrium level to zero at or below the LFC or above the storm top. Although the inequality constraint has been implemented to evaluate the overall reliability of integrated divergence in the wind analyses, the inequality constraint algorithm does not impose any wind analysis adjustments in the 9 June case, since the derived vertical velocities are well within parcel buoyancy limits.

c. *Temporal adjustment of radar analysis fields for storm motion*

One or more of the Doppler radars that contribute to a series of dual- or multiple-Doppler analyses may collect data volumes in a different time sequence than the subset of radars whose volumes are obtained at the chosen radar analysis times (the former being termed "nonsynchronized" radars in the present study). To effect multiple-Doppler wind synthesis at a common analysis time, a simple single-radar "time morphing" algorithm has been developed to produce synthetic synchronized single-radar analyses (e.g., V_r and Z_H) from a time series of nonsynchronized single-radar analyses. Applying the spatial and temporal interpolation procedures described in section 2b of Z13, the gridpoint fields from a pair of two consecutive nonsynchronized single-radar objective analyses are each shifted to the desired intermediate analysis time via an advection correction using a constant vector storm motion (e.g., Fig. 1). The application of a constant storm motion via the time-morphing scheme contrasts with the approach of Shapiro et al. (2010), who instead adopt a variational approach to calculate a spatially variable reference frame motion vector. The advection-corrected gridpoint fields from each time-spaced analysis are then mapped back to the fixed radar analysis grid domain via bilinear spatial interpolation. The subsequent linear temporal weighting of the advection-corrected, spatially interpolated gridpoint values from each analysis produce the final synthetic 3D single-Doppler analysis field (Fig. 1).

A multiple-Doppler version of the time-morphing algorithm manages the time-to-space relocation of a dual- or multiple-Doppler radar analysis to a new effective analysis time assuming a steady-state structure following the storm motion (e.g., Fig. 1 and caption). The gridded multiple-Doppler analysis fields are moved with the storm motion vector and bilinearly interpolated to the fixed analysis grid domain without amplitude change. This option is useful for extending the effective time period over which backward trajectories may be integrated to assist them in reaching either the storm's environment or the boundaries of the analysis domain.

d. *Scaling graupel concentration with observed evolution of storm intensity*

The graupel concentration field may be optionally scaled to reflect the changing intensity of an analyzed storm as inferred, for example, from evolving peak updraft strength or maximum reflectivity (Z13). The scaled concentration is computed as $N_g = \alpha_N N_g^0$, where N_g^0 is

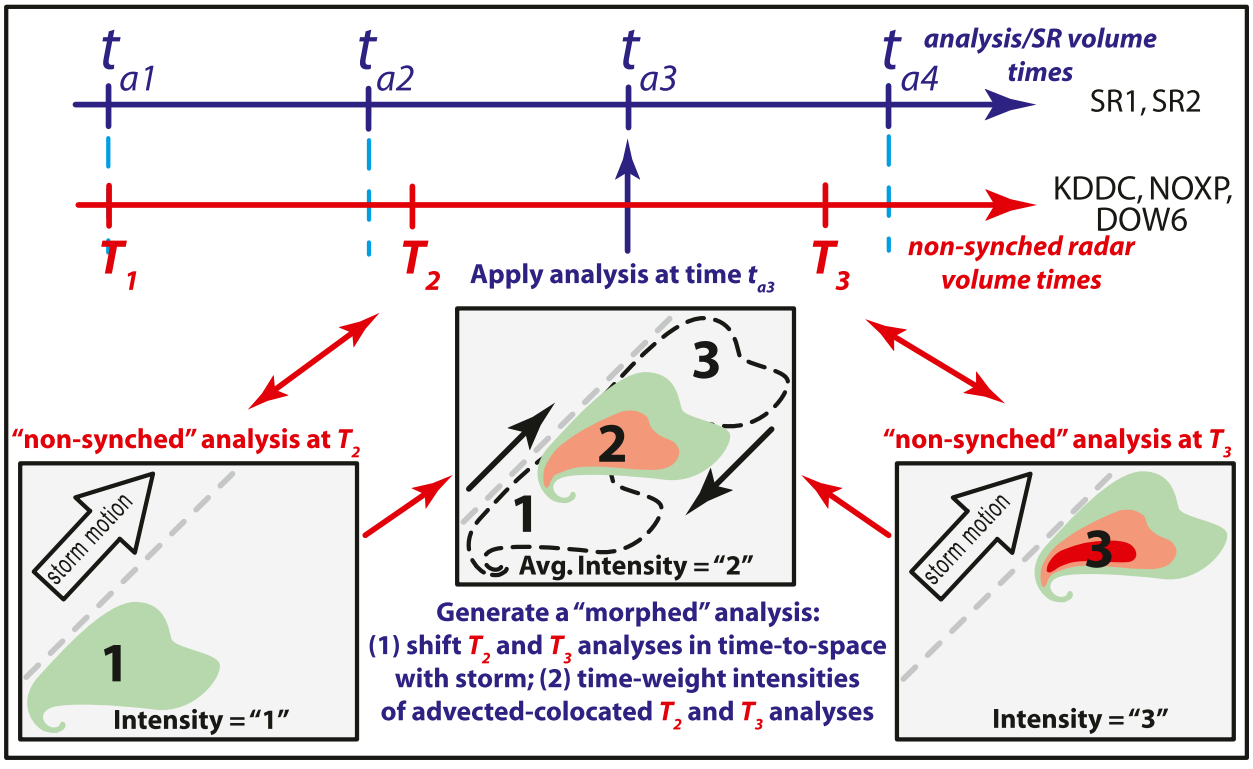

FIG. 1. Conceptual diagram of the time-morphing technique used to map two consecutive, nonsynchronized single-radar analyses to a common analysis time. For the special case of multiple-Doppler radar analyses in the period $t_{a1} \le t \le t_{a4}$, an option of the time-morphing technique allows the user to expand the effective analysis period by time shifting the position of an analysis either backward (e.g., $t_a < t_{a1}$) or forward (e.g., $t_a > t_{a4}$) with the storm motion assuming local steadiness.

the unscaled graupel concentration and $\alpha_N = \alpha_N(t)$ is an input graupel concentration scaling parameter. For the 9 June case, a linear time variation of α_N was assumed between the storm's late-mature stage at approximately 2342 UTC and its early decay stage at approximately 0000 UTC 10 June (hereafter all times are UTC), while constant α_N was assumed for earlier and later times (Table 1). An analysis test assumes the default value of $\alpha_N = 1$ to assess the impact of not scaling N_g because of a lack of information on evolving storm intensity.

e. Impact of unsampled near-surface radial velocities on low-level radar-synthesized winds

The potential negative impacts of poor spatial sampling density of radial velocity observations on multiple Doppler wind fields have long been recognized (e.g., Ray et al. 1980a), of which one example is absence of near-surface radial velocity observations below the base-scan elevation. As described further in section 3a, the present study improves low-level radar sampling by combining observations from three storm-scale radars at relatively long range with two mesocyclone-scale radars at close range to the storm core (thereby augmenting low-altitude observations). Unfortunately, independent measurements of the true 3D wind field with which to quantify the impact of coarse radial velocity sampling at low elevation angles on multiple-radar estimates of the low-level airflow do not exist. An alternative method for providing high-resolution wind information to test radar analysis techniques is the "radar emulator" approach, according to which high-resolution simulated storm output fields are sampled using appropriate weighting functions to create proxy radar fields (e.g., May et al. 2007; Wood and Brown 1997) from which the wind field may be approximated using conventional Doppler wind synthesis methods (e.g., Majcen et al. 2008). The following simplified error analysis considers only the impact of radar beam averaging and downward extrapolation below the lowest data-bearing level while neglecting other effects of the spatial interpolation and wind synthesis algorithms.

Since the Binger storm simulation utilized by Z13 has a rather coarse grid spacing intended to resolve storm-scale airflow features, a high-resolution simulation of the 29 May 2004 Geary, Oklahoma, supercell (E. Mansell 2013, personal communication) is employed via a very simple radar emulator approach to compare modeled horizontal winds and horizontal divergences through

TABLE 1. List of parameters contained in diagnostic relationships for precipitation quantities in the DLA. (See Z13 for a description of the precipitation diagnostic approach as well as the microphysical, perturbation surface-layer downdraft, damping, and surface flux parameterizations employed by the DLA.) The symbols and values of the various parameters are also listed. Time t has units of floating-point hours after 0000 UTC 9 Jun 2009 for the Greensburg storm case. The time-varying graupel concentration scale $\alpha_N(t)$ is held constant at 0.5 and 1.7 for $t < 23.7$ and $t > 24.0$, respectively, and varies linearly for $23.7 < t < 24.0$.

Parameter (units)	Symbol	Value
Coefficient in Z_{er} expression	C_r	1×10^{18}
Coefficient in Z_{eg} expression	α_r	0.224
Coefficient in Z_{eg} expression	C_g	7.295×10^{19}
Coefficient in regression for q_r	ε_r	0.5
Coefficient in regression for q_g	ε_g	1.0
Coefficient in regression for n_{0g} (m^{-4})	$(n_{0g})_0$	3.355×10^5
Rain intercept parameter (m^{-4})	n_{0r}	8×10^5
Coefficient in Eq. (7) for V_r ($m\,s^{-1}$)	a_r	10
Coefficient in Eq. (7) for V_r (m^{-1})	f_r	516.575
Density of water ($kg\,m^{-3}$)	ρ_w	1000
Graupel density ($kg\,m^{-3}$) at 5 km AGL	ρ_g^{5km}	630
Graupel density ($kg\,m^{-3}$) at surface	ρ_g^{sfc}	690
Environmental melting level height (km AGL)	H_{melt}	3.7
Height (km AGL) of −15°C in updraft core	H_{frz}	7.1
Bigg freezing coefficient in C_{frz} (see text)	α_{frz}	0.1
Updraft threshold ($m\,s^{-1}$) for onset of recycling	W_{min}	5
Updraft threshold ($m\,s^{-1}$) for $q_g = 0$ below H_{melt}	W_{max}	20
Constant N_g scale	α_N	1
Time-varying N_g scale	$\alpha_N(t)$	0.5–1.7 ($23.7 \le t \le 24.0$)

the lowest several hundred meters above ground. The Geary storm simulation has employed the Collaborative Model for Multiscale Atmospheric Simulation (COMMAS) model following the general methods described by Mansell et al. (2010) and Mansell and Ziegler (2013), and includes multimoment liquid- and ice-phase parameterized microphysics. A sounding obtained during the 2004 Thunderstorm Electrification and Lightning Experiment (TELEX-2004; MacGorman et al. 2008) represents the strongly unstable ambient inflow environment [assumed horizontally homogeneous with mixed-layer convective available potential energy (MLCAPE) ~3000 J kg^{-1}] to the southeast of the Geary storm at 2237. The model domain is 100 km × 125 km horizontally and extends from the surface to 24 km AGL. The horizontal grid spacings are $\Delta x = \Delta y = 125$ m, while the vertical grid spacing is stretched from $\Delta z =$ 100 m at the surface to 700 m above 15 km AGL. The simulated Geary storm is a classic supercell at 2 h with a similar storm-scale structure to the simulated Binger storm at 4 h 40 min (Ziegler et al. 2010). The simulated Geary storm has a maximum updraft of about 60 m s^{-1}, a peak reflectivity of about 70 dBZ, and a very intense low-level tornado-cyclonic circulation with a peak vertical vorticity of about 0.7 s^{-1} associated with the mesocyclonic main updraft.

Horizontal proxy radar winds and horizontal divergences were estimated at 50 m (i.e., grid level $k = 1$) and 257 m AGL ($k = 3$) using a simple radar emulator and compared to assess the validity of extrapolating horizontal wind from the elevation of the lowest sweep to ground level. The wind components were destaggered to the model's scalar points from the Arakawa C grid. Assuming for simplicity a storm-scale radar with a 1° half-power beamwidth whose radial coincides with the velocity component being emulated (i.e., ray locally parallel to grid row or column for the u or v component, respectively), a gate located at 25-km range and 0.6° elevation (for which the gate height is ~260 m) for each grid point, and considering grid points with simulated reflectivity greater than 10 dBZ, the grid-level proxy radar horizontal wind components (u_r, v_r) are estimated from model-output wind components (U, V) at $k = 3$ via the expressions

$$u_r = (\omega_{bc} U_{i,j,k} + \omega_{bekm} U_{i,j,km} + \omega_{be} U_{i,j,kp} + \omega_{be} U_{i,jm,k} + \omega_{be} U_{i,jp,k})/(\omega_{bc} + n\omega_{be}) \quad (1)$$

and

$$v_r = (\omega_{bc} V_{i,j,k} + \omega_{bekm} V_{i,j,km} + \omega_{be} V_{i,j,kp} + \omega_{be} V_{im,j,k} + \omega_{be} V_{ip,j,k})/(\omega_{bc} + n\omega_{be}), \quad (2)$$

where the subscripts m and p following a grid index i, j, or k denote an increment of "−1" and "+1," respectively, for that index; the beam-center weight $\omega_{bc} = 1$ and the beam-edge weights $\omega_{be} = \omega_{bekm} = 0.5$ (e.g., Wood and Brown 1997); and $n = 4$. Since the radar sample is effectively restricted to the upper half of the beam for the radar measurement at 50 m, Eqs. (1) and (2) are evaluated with $\omega_{bekm} = 0$ and $n = 3$ at $k = 1$. Since the edge of the main lobe overlaps between the two levels, the radial velocity measurements are effectively oversampled. The pseudoradar horizontal divergence is then calculated from $\partial u_r/\partial x + \partial v_r/\partial y$ at each level using standard centered finite differencing.

The resulting correlations of the bilevel radar-emulated fields suggest that rather modest errors are generally incurred by extrapolating the horizontal radar wind

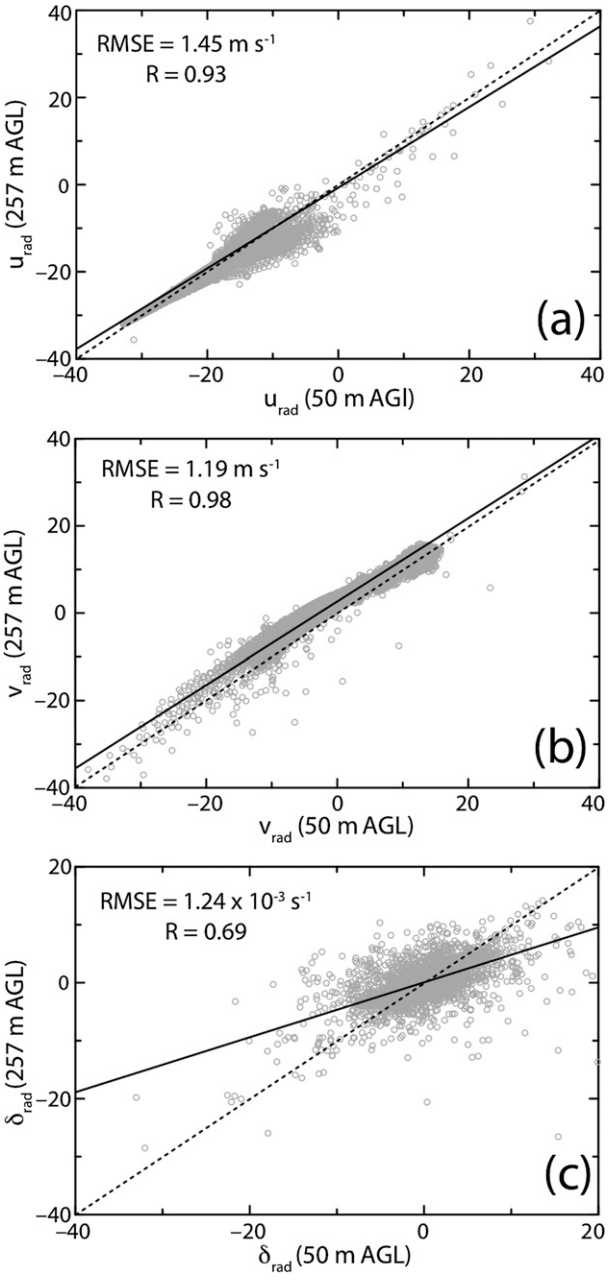

FIG. 2. Scatterplots of radar-emulated horizontal winds and horizontal divergence at the 50-m vs the 257-m grid level of the simulated 29 May 2004 Geary supercell storm at 2 h showing (a) u_r ($m\,s^{-1}$), (b) v_r ($m\,s^{-1}$), and (c) horizontal divergence δ_r ($10^{-3}\,s^{-1}$). The quantities on the panel axes are labeled with a subscript "rad" to emphasize their derivation from equivalent model-output quantities with the simple radar emulator described in the text. The quantities *R* and RMSE correspond to the indicated linear regression fit (black line).

components and horizontal divergences from the level of the lowest radar sweep to ground level (Fig. 2). Radar-averaged wind speed differences between the levels are typically of order $1\,m\,s^{-1}$ (although some grid columns have differences exceeding $\sim 5\,m\,s^{-1}$), while the bilevel wind components are highly correlated with RMS deviations of only $\sim 1\,m\,s^{-1}$. Although the scatter of horizontal divergence values suggests fairly good agreement between values at 50 and 257 m, the downward-extrapolated horizontal divergence as inferred from the regression line may be low biased by up to order $5 \times 10^{-3}\,s^{-1}$ (equivalent to an approximately $0.5\,m\,s^{-1}$ vertical velocity error over the lowest 100 m) for characteristic divergence magnitudes of order $10 \times 10^{-3}\,s^{-1}$. As demonstrated by Ray et al. (1980b), the latter incrementally integrated divergence error is equivalent to a negligible lower boundary condition error via the gradual accumulation of vertical velocity error variance accompanying the vertical integration of the mass continuity equation from the ground through storm midlevels (see also section 2b). The above-mentioned wind differences would decrease with decreasing radar range and increase with decreasing beamwidth (i.e., with weaker beam averaging). Finally, the previously mentioned oversampling in low levels provided by two pencil-beam mobile radars at close range (see section 3a) in combination with multiple storm-scale radars at greater range is expected to reduce potential horizontal wind and divergence errors near the surface in the radar-analyzed Greensburg storm.

3. Application of the DLA to a radar-observed storm

a. Radar analysis and trajectories in the 9 June 2009 Greensburg, Kansas, storm

Time-dependent 3D vector airflow and reflectivity fields have been obtained from multiple-Doppler syntheses of observations of the 9 June 2009 Greensburg, Kansas, supercell from up to five radars employing the overdetermined dual-Doppler analysis method previously described in section 2b. Data from four mobile radars, including the Shared Mobile Atmospheric Research and Teaching (SMART) radars SR1 and SR2 (Biggerstaff et al. 2005), the National Oceanic and Atmospheric Administration (NOAA) National Severe Storms Laboratory (NSSL) X-band polarimetric (NOXP) radar (Burgess et al. 2010; Schwarz and Burgess 2010), and the Doppler-on-Wheels 6 (DOW6; Wurman et al. 1997; Wurman 2001) that were all deployed in support of VORTEX2, are combined with data from the Weather Surveillance Radar-1988 Doppler (WSR-88D) at Dodge City, Kansas (KDDC). Radars are located relative to the Greensburg storm as depicted in Fig. 3b (see also Fig. 5 of Wurman et al. 2012). The time-morphing procedure described in section 2c has been employed to

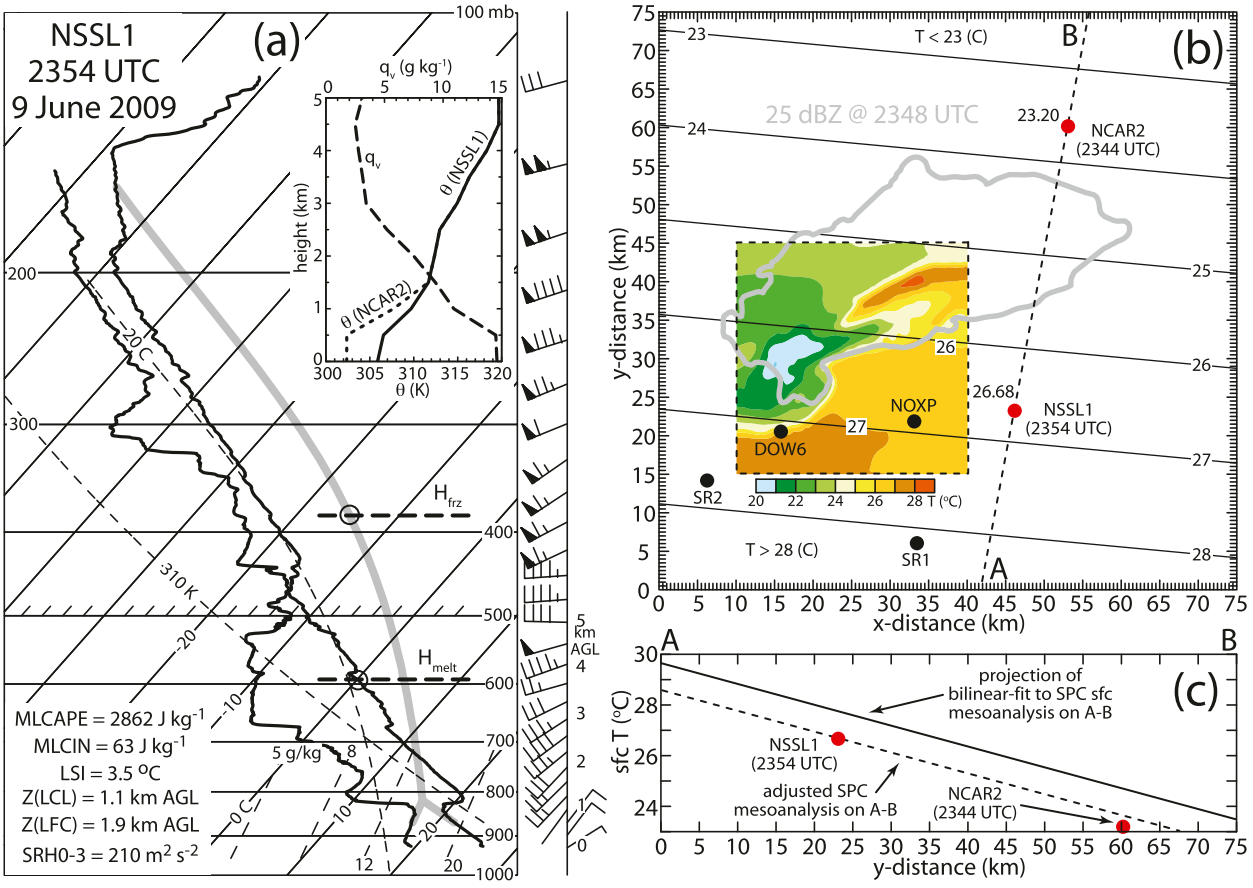

FIG. 3. Mesoscale environment of the 9 Jun 2009 Greensburg storm as input into the DLA. (a) Skew T–log$p$ plot of the NSSL1 mobile sounding used to define the shape of the vertical profiles in the storm environment; (b) mesoscale environmental surface temperature (K) in the radar analysis domain (black lines), with inset, color-filled surface temperature at 2348 from the control DLA described in the text; and (c) projection of surface temperature (K) vs y distance (km) in the radar analysis domain along the dotted line AB in (b). The 2354 UTC NSSL1 sounding described in the text was launched at $(x, y) = (46, 23)$ km in radar analysis coordinates. The locations of the soundings and mobile radars are indicated by red and black dots, respectively, in (b), while KDDC is located at $(-23, 41)$. The inset in (a) depicts (i) the environmental θ and q_v profiles (solid and dashed curves, respectively) that were input into the DLA and mesoscale environmental analysis from the NSSL1 sounding; and (ii) the θ profile from the 2344 UTC National Center for Atmospheric Research mobile sounding (NCAR2; dotted curve). The q_v profile in the inset of (a) was similar in the NCAR2 and NSSL1 soundings. Altitudes H_{melt} and H_{frz} are described in the text and listed in Table 2. The 0–3-km storm-relative helicity (SRH0–3) is computed relative to the estimated storm motion of $(u_s, v_s) = (12, -2)$.

synchronize the data volumes from the latter three radars (NOXP, DOW6, and KDDC). An attenuation correction based on the ZPHI method (Testud et al. 2000) has been applied to the NOXP reflectivity data (e.g., Schwarz and Burgess 2010). The dimensions of the fixed analysis grid are 75 km × 75 km in the horizontal and 18 km in altitude with a uniform grid spacing of 0.5 km in all directions. The large dimensions of the analysis domain and corresponding large peak radar ranges commend a rather conservative choice of $\Delta \approx 1.05$ km, which yields a Barnes filtering parameter value of $\kappa \approx 1.94$.

The DLA has been applied within the time period spanned by a series of multiple-Doppler analyses. The radar analyses have been generated at a 3-min interval from 2342 on 9 June to 0024 on 10 June 2009, and range from triple Doppler at 2242 and 0018–0024 up to quadruple Doppler at 2345–2357 and 0015 and quintuple Doppler in the period 0000–0012. Rather weak evolution of storm-scale radial velocity and reflectivity fields from KDDC between 2300 and 2342 supports the hypothesis that storm features larger than the scale of the low-level mesocyclone were quasi steady during the latter period. The time-morphing technique described in section 2c has been employed to spawn synthetic u, v, w, and Z_H fields spaced at a 3-min interval in the period 2300–2339 using the 2342 triple-Doppler wind synthesis and assuming a steady-state storm structure. The DLA has been implemented in a nested 30 km × 30 km × 5 km analysis domain with a grid spacing of 0.5 km in all

directions, yielding a total of 40 931 backward trajectories. Because of the areal extent and motion of the storm in the fixed radar analysis domain, somewhere in the range of about 40 430–40 910 backward trajectories (i.e., 98.78%–99.95% of all trajectories) reach the storm environment as defined by the conditions described in section 2a of Z13. A storm motion of $(u_s, v_s) = (12, -2)$ m s^{-1} is assumed in the single-radar objective analyses and the position adjustments of the radar analyses via time morphing. The ground-relative trajectory calculations employ a time step of $\Delta t = 20$ s.

b. Heterogeneous storm environment

The temperature T, dewpoint temperature T_d, and $p_B(z)$ of the inflow environment to the south of the storm has been profiled by the NSSL1 mobile sounding system about 8 miles east of Greensburg, Kansas, at 2354 (Fig. 3a). The surface T field from the NOAA Storm Prediction Center (SPC)'s mesoanalysis is closely approximated by a bilinear 2D polynomial fit that spans the radar analysis domain (Fig. 3b) and is scaled to NSSL1's surface T value (Fig. 3c). Both the $T(z)$ values at and above 1.5 km AGL and the pressure and $T_d(z)$ values at all levels are prescribed from the NSSL1 sounding. Environmental θ values are calculated from T using p_B (Z13), and p_B has a surface value of 930.2 mb. The surface heat flux value that maintains the stationary surface θ field with the observed surface vector wind from NSSL1 has been computed via Eq. (28) of Z13 as $\dot{\Theta} = \mathbf{V}_h \cdot \nabla\theta|_{\text{sfc}} = 0.45$ K s^{-1}. The surface q_v flux is neglected in this study.

A simplified analytic version of variational "shape matching" (McGinley 1982) is used to derive the horizontal T field at intermediate grid levels between the known surface and 1.5-km values in each grid column. The T values at intermediate levels are constrained by equating the second vertical derivatives of the local T profile to the proximity sounding at the same level. The governing relations to be solved take the form

$$T(2) = [T(3) + T(1) - \nabla^2_{\text{zo}}|_2]/2 \tag{3}$$

for $z = 0.5$ km (level 2) and

$$T(3) = [T(4) + T(2) - \nabla^2_{\text{zo}}|_3]/2 \tag{4}$$

for $z = 1$ km (level 3), where the vertical Laplacian operator at each level is prescribed from its value ∇^2_{zo} in the proximity sounding. It follows that

$$T(2) = (4/3)\{[T(4) - \nabla^2_{\text{zo}}|_3]/4 + [T(1) - \nabla^2_{\text{zo}}|_2]/2\} \tag{5}$$

and

$$T(3) = (4/3)\{[T(1) - \nabla^2_{\text{zo}}|_2]/4 + [T(4) - \nabla^2_{\text{zo}}|_3]/2\}, \tag{6}$$

where the values $T(2)$ and $T(3)$ are determined from the known T values at the surface and 1.5 km and the sounding-derived Laplacian values at the intermediate levels.

c. DLA test results for the Greensburg storm

The surface-level DLA output has been validated against surface in situ measurements from mobile mesonet and StickNet platforms (Wurman et al. 2012) that were deployed in the path of the Greensburg storm (Fig. 4). The mobile mesonet vehicles derive from the successful design developed by Straka et al. (1996) and subsequently modified for the 2002 International H_2O Project (IHOP-2002; Ziegler et al. 2004) and VORTEX2 (Waugh and Fredrickson 2010). StickNets are tripod-mounted weather stations that are deployed along roads ahead of the storm and left in place as the storm traverses the array (Weiss and Schroeder 2008; Skinner et al. 2011). The Lagrangian-analyzed θ_v are reasonably well correlated with the surface θ_v observations (Fig. 4a) as indicated by R, standard deviation σ, and RMSE of 0.77, 1.4, and 1.1 K, respectively. Although the q_v points tend to cluster around the q_v values of the moist inflow boundary layer (BL) (e.g., Fig. 3a inset), thereby contributing to a reduced linear correlation, the q_v points nevertheless exhibit acceptably small σ and RMSE values of 1 and 0.74 g kg^{-1}, respectively (Fig. 4b). Although the in situ observations are predominantly from the storm's surface precipitation core and cold outflow, their RMSE values nevertheless are broadly consistent with the OSSE test results through the lowest 5 km of the simulated Binger storm (i.e., 0.83 K and 0.56 g kg^{-1} in Figs. 6a and 6b of Z13).

A subjective analysis of the difference between the time-spaced surface DLA outputs and in situ measurements is broadly suggestive of spatial error patterns in the sense of a time-to-space data conversion following the storm's motion (Fig. 5). Inferring possible spatial patterns of analysis error is challenging because of the spatial sparseness of the in situ observations, the differing resolutions of the DLA and the in situ sensors, and a gradual storm decay after 2348, which implies the possibility of nonstationary time series of the observed variables. A composite surface radar analysis of $\mathbf{V}_h$ and Z_H was constructed by advecting each radar analysis to the storm's position at 0003 via the time-morphing algorithm (described in section 2c) and computing the gridpoint arithmetic weighted-average values of the advected analyses. The composite radar analysis

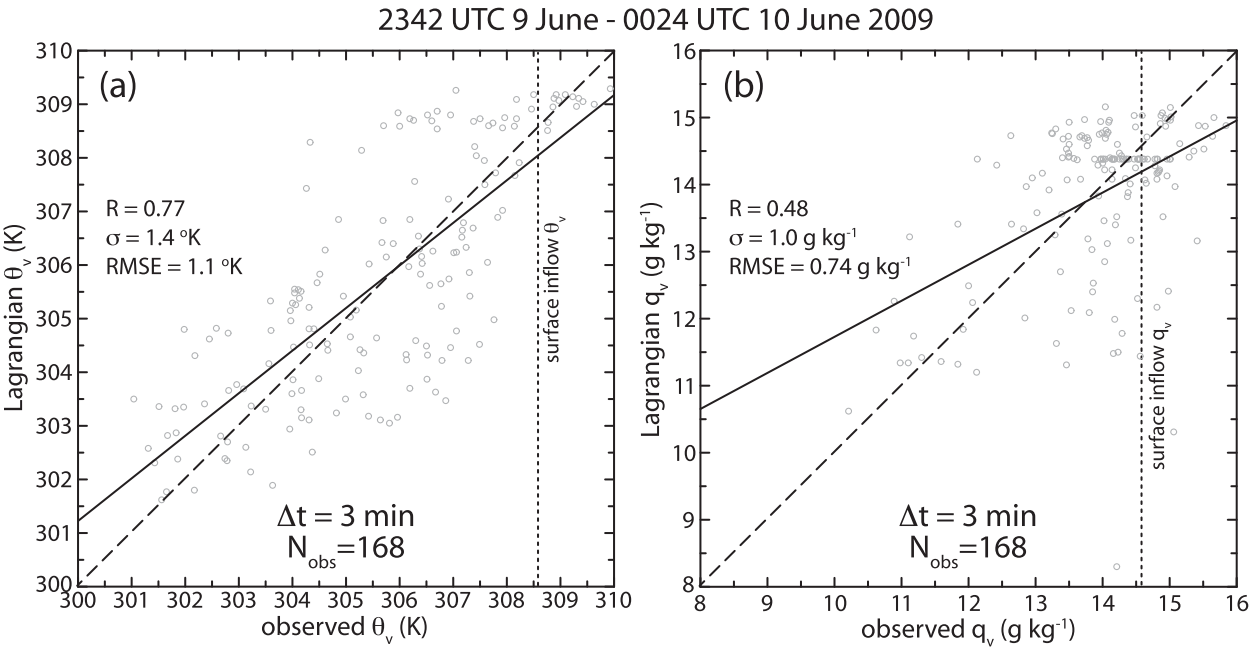

FIG. 4. Scatterplots of surface conditions from in situ observations provided by mobile mesonet and StickNet probes vs 3-min interval surface DLA values (i.e., that were bilinearly interpolated to the individual probe sites) in the Greensburg storm from 2342 UTC 9 Jun to 0024 UTC 10 Jun 2009. Shown are (a) θ_v (K) and (b) q_v (g kg^{-1}). The quantities R, σ, and RMSE correspond to the indicated linear regression fit (black line).

provides a morphological context to help interpret the local DLA error values that have been advected in time to space in the same manner as the radar analyses. A concentrated warm anomaly (i.e., positive $\Delta\theta_v$ = DLA $\theta_v >$ measured θ_v) is located in the forward-flank rain area and a smaller warm anomaly is located in the forward-flank inflow east of the hook echo (Fig. 5). Two concentrated cold anomalies are located in the rear-flank downdraft (RFD) precipitation core and the RFD outflow west of the storm. However, the overall storm area is dominated by local $\Delta\theta_v$ values of either sign that are less than 1 K in magnitude (i.e., consistent with RMSE = 1.1 K from Fig. 4a).

A series of DLA tests (and test category acronyms are in Table 2) display varying sensitivity in comparison to the optimally robust CNTL analysis (Fig. 6). Analysis CNTL produces a strong, expansive cold pool with a minimum $\Delta\theta_v$ as low as −7.5 K centered on the western flank of the reflectivity core in good agreement with in situ measurements (Fig. 6a). The storm core of CNTL (Fig. 6b) reveals the cold pool through the lowest 1–2 km, a locally warm precipitation-filled RFD centered at a horizontal distance of 10.5 km in the cross section and z = 2 km, and a strongly buoyant updraft centered at a horizontal distance of 14.5 km in the cross section above 2.5 km, whose cloud base and level of neutral buoyancy approximate the environmental LCL and LFC, respectively (e.g., Fig. 3a). The negatively buoyant updraft base and flanks are diluted by entrainment from the evaporatively chilled cold pool (Rotunno and Klemp 1985) and the drier ambient middle levels (Fig. 6b). Analysis 1SND effectively concentrates the cold pool in the reflectivity core and rear-flank outflow region (Fig. 6c), and helps gauge the impact of horizontally heterogeneous BL temperatures via comparison with CNTL. Analysis NGSC (Fig. 6d), which deactivates scaling of graupel concentration, produces a slightly weaker cold pool than CNTL by sustaining slightly reduced graupel total concentrations and decreased diabatic cooling from graupel melting. Analysis GMLT heavily suppresses cold pool intensity (Fig. 6e) resulting from elimination of diabatic cooling from graupel melting in the midlevel downdrafts, with rain evaporation providing the bulk of diabatic cooling. Conversely, analysis RVAP suppresses cold pool intensity relative to GMLT rather weakly in the RFD and rather strongly in the forward-flank rainy downdraft (FFD) (Fig. 6f versus Fig. 6e). Hence, considering GMLT and RVAP in relation to CNTL implies the important combined role of rain evaporation and graupel melting to form and maintain the storm's cold pool. An interesting aspect of analysis RVAP is the presence of unobserved warm surface temperatures in the FFD (analogous to the localized warm anomaly in the FFD in

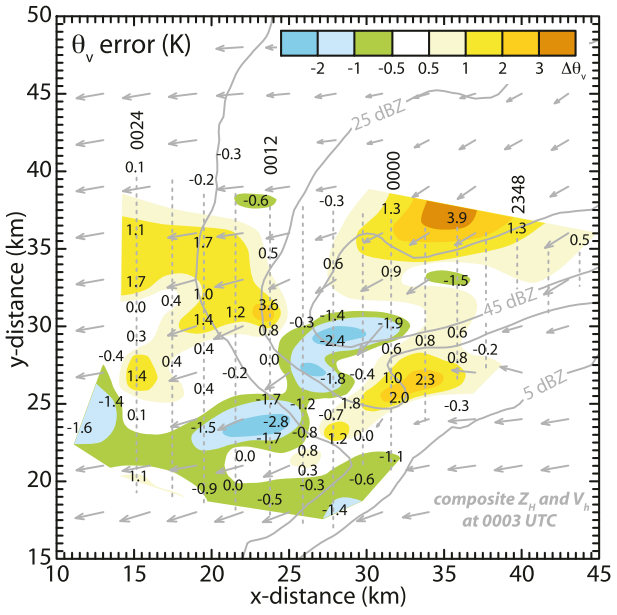

FIG. 5. Subjective analysis of surface virtual potential temperature difference $\Delta\theta_v'$ (K) obtained by subtracting in situ observations obtained in the period 2342–0024 from their equivalent DLA values in the Greensburg storm on 9–10 Jun 2009. The DLA-output values were spatially interpolated to corresponding locations of an observation at the analysis times to compute the discrete $\Delta\theta_v'$ values. Plotted values correspond to $\Delta\theta_v'$ of selected mobile mesonet and StickNet observations. Also shown are isochrones of the south–north StickNet array at the indicated analysis times (vertical dotted gray lines), the composite surface radar analysis described in the text (Z_H, gray contours), and horizontal storm-relative airflow (gray vectors).

Fig. 5), thus emphasizing the importance of rain evaporation to locally counter adiabatic warming following shallow boundary layer trajectories that process through the FFD. Analyses NOCOL, NOLD, and WSFC produce very similar sensitivities to their corresponding OSSE tests (not shown).

d. DLA-derived surface rain rate in the Greensburg storm

To help assess uncertainties regarding the assumed form of the rain drop size distribution and the method for diagnosing precipitation content via the DLA, the surface rain rate has been derived from the DLA output and compared to an independently measured accumulated surface rainfall in the Greensburg storm. Since the DLA diagnoses rather than predicts rain and graupel contents from Z_H, an asymptotic form for the relationship between rain fall speed and diameter is adopted that broadly follows Atlas et al. (1973) and Kumjian and Ryzhkov (2012) via fitting of the Gunn and Kinzer (1949) rain fall speed data. The resulting empirical relationship for rain drop fall speed versus diameter is

TABLE 2. Sensitivity tests of the DLA. The CNTL case includes all source and sink terms, the heterogeneous environment described in the text, the microphysical and precipitation-diagnostic parameters listed in Table 1, and the perturbation surface-layer downdraft, damping, and surface flux parameters listed in Table 1 of Z13. The sensitivity tests all vary only one term or parameter, but otherwise are identical to CNTL.

Analysis test category	Acronym	Attributes or differences vs CNTL
Control	CNTL	All physics/heterogeneous environment
Homogeneous environment	1SND	Single inflow sounding
Graupel melting	GMLT	No graupel melting
Scaled graupel concentration	NGSC	$\alpha_N = 1.0$
Rain and graupel collection of cloud water	NOCOL	No cloud collection
Lagrangian damping	NOLD	No damping
Rain evaporation	RVAP	No rain evaporation
Near-surface downdraft	WSFC	No surface downdraft

$$V_r = a_r[1 - \exp(-f_r D_r)], \tag{7}$$

where D_r is rain drop diameter (m) and a_r and f_r are empirically derived coefficients listed in Table 1 (E. Mansell 2013, personal communication). The mean rain drop fall speed ($\mathrm{m\,s^{-1}}$) is derived by integrating the product of Eq. (7) and the rain drop size distribution (Z13) over all D_r and takes the form

$$\overline{V}_r(\overline{D}_r) = (1.225/\rho_{\mathrm{sfc}})^{0.5} a_r[1 - (1 + f_r\overline{D}_r)^{-4}], \tag{8}$$

where ρ_{sfc} is surface air density ($\mathrm{kg\,m^{-3}}$) and $\overline{D}_r = \lambda_r^{-1}$ is the concentration-weighted mean drop diameter (m) obtained from the local rain distribution (Z13). The DLA-derived instantaneous surface rain rate R_{DLA} ($\mathrm{mm\,h^{-1}}$) is computed as

$$R_{\mathrm{DLA}} = 3.6 \times 10^6 (\rho_{\mathrm{sfc}} q_r \overline{V}_r / \rho_w), \tag{9}$$

where rain mixing ratio q_r ($\mathrm{kg\,kg^{-1}}$) is diagnosed by the DLA (Z13), $\overline{V}_r$ is computed from Eq. (8), and ρ_w is listed in Table 1. It should be noted that because of the kinematic lower boundary condition $w = 0$ (section 2b), the surface rain rate from the DLA is independent of the radar wind analysis (and vertical velocity in particular) and varies only with H_{melt} via the partitioning of Z_H between q_r and q_g (Z13).

The DLA-derived instantaneous surface rain rates in the +50-dBZ reflectivity core exceed 30–45 $\mathrm{mm\,h^{-1}}$ with significant areal coverage exceeding 150 $\mathrm{mm\,h^{-1}}$ and a peak value exceeding 250 $\mathrm{mm\,h^{-1}}$ (Fig. 7, Table 3). The DLA-estimated rain rate at constant, high Z_H may locally vary across the range of values of 100–200 $\mathrm{mm\,h^{-1}}$

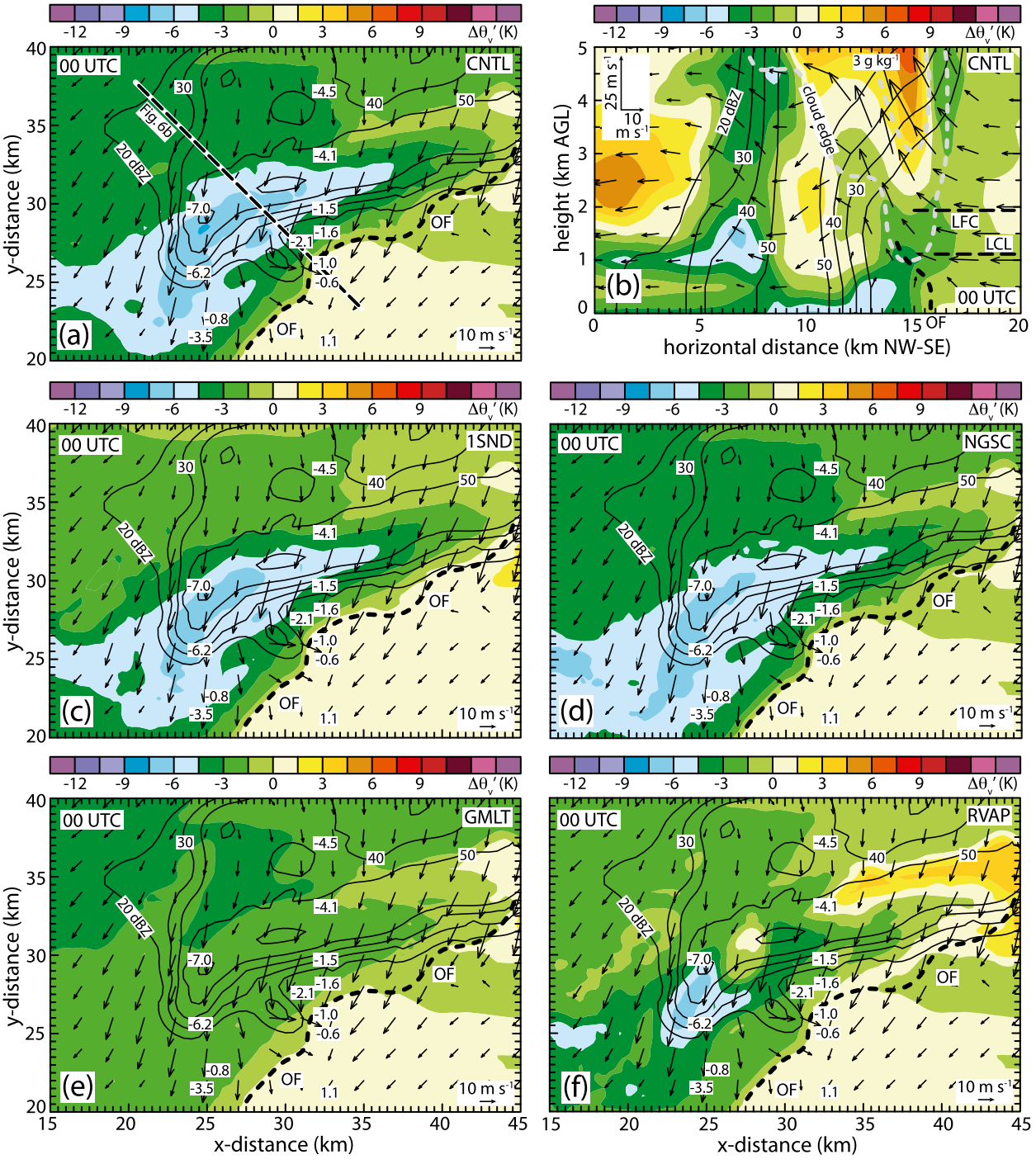

FIG. 6. Surface virtual potential temperature deviation from the environment $\Delta\theta_v'$ (K) from DLA of the Greensburg storm at 0000 UTC 10 Jun 2009. The results for different analysis tests are depicted as follows: (a) CNTL; (b) vertical northwest–southeast cross section through CNTL located in (a); (c) homogeneous environment; (d) graupel concentration scaled by a constant $\alpha_N = 2$ (see text); (e) no graupel melting; and (f) no rain evaporation. Analyses (c)–(f) all utilize the same single inflow environmental sounding (NSSL1 at 2354 UTC 9 Jun). Vectors are horizontal, domain-relative airflow except for (b) (storm relative). The black contours depict Z_H (dBZ), while the dashed gray contours in (b) denote the cloud edge and $q_c = 3\,\mathrm{g\,kg^{-1}}$. The black dashed curve and OF denote the leading edge of the surface outflow as located in (a).

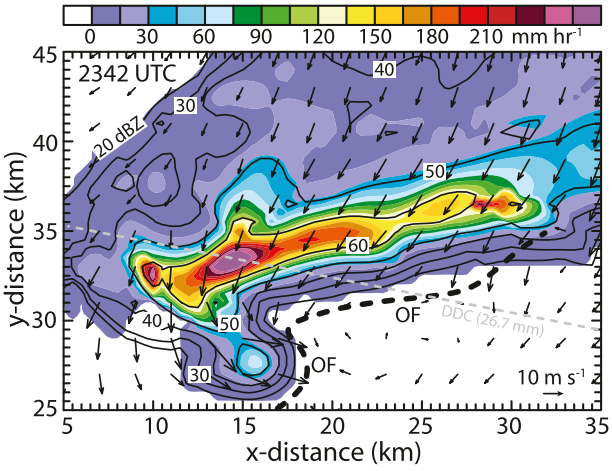

FIG. 7. Analysis of instantaneous surface rain rate (mm h^{-1}) in the 9 Jun 2009 Greensburg storm from the DLA at 2342. The surface radar analysis is depicted by Z_H (black contours) and horizontal, ground-relative airflow vectors. The gray dashed line denotes the trajectory of the National Weather Service (NWS) hourly precipitation gauge at Dodge City Regional Airport (26.7 mm total accumulation) relative to the Greensburg storm motion. The black dashed curve and OF denote the leading edge of the surface outflow from CNTL at 2342.

(e.g., following the 60-dBZ contour in Fig. 7) because of the variable partitioning of Z_H between q_r and q_g (Z13). Although conventional operational radar-derived instantaneous surface rain rates (e.g., Zhang et al. 2011) may be capped above roughly 80 mm h^{-1} (thus inhibiting direct comparison of rain rates from the DLA and nonpolarimetric operational radar measurements), the incorporation of polarimetric variables holds considerable promise for improving instantaneous and accumulated radar rainfall estimates (e.g., Vasiloff 2012) that could ultimately help validate DLA-derived fields in future studies.

The DLA-derived instantaneous surface rain rates at 2342 have been compared to the accumulated rainfall from the passage of the Greensburg storm (Fig. 7). A total rainfall accumulation $A = 26.7$ mm was measured by an operational catchment gauge located at Dodge City (Fig. 7). The storm-total precipitation P is related to the mean rainfall rate $\overline{R}$ (mm h^{-1}) and duration D (h) by the expression $P = \overline{R}D$ (Doswell et al. 1996). A rain-rate profile $R(t) = 4.86 \exp(t/3.8)$ has been fit to the space-to-time-converted DLA-derived values in the time subintervals before and after the peak rainfall rate $M \sim 255$ mm h^{-1} along the dashed line in Fig. 7 (e.g., Doswell et al. 1996), where t is time (min) increasing from zero at the eastern or western storm edges to the time of the peak rate M and $R(t)$ has units of millimeters per hour. An event duration of approximately

TABLE 3. Storm area exceeding various threshold values of instantaneous rain rate (mm h^{-1}) as estimated from the DLA-diagnosed surface rain-rate field at 2342 in the 9 Jun 2009 Greensburg storm. A gridcell area of 0.25 km^2 is used to compute total area from the number of grid cells. The value of Y (km) is the estimated dimension of the region enclosed by the indicated rain rate in the direction normal to the storm motion.

Instantaneous rain rate (mm h^{-1})	Number of grid cells	Area (km^2)	Areal dimension normal to storm motion Y (km)
10	1128	282	>20
50	348	87	12.5
100	200	50	9.5
150	102	26	7
200	32	8	2
250	8	2	1.5

$D = 30$ min is broadly consistent with the Greensburg storm's along-track dimension (~20 km) and average observed motion speed (~12 m s^{-1}). The mean rainfall rate has been calculated by integrating $R(t)$ over $D/2 = 15$ min and dividing the integral by 15 min, yielding $\overline{R} = 62$ mm h^{-1} and a DLA-derived P value of about 31 mm, which compares favorably to the observed accumulation A. Given a gauge measurement of at least 10 mm h^{-1}, and considering the computed areas exceeding various instantaneous DLA-estimated rain-rate thresholds (Table 3) and the rain core's dimension normal to the storm motion (Fig. 7), the indicated gauge had an estimated a posteriori probability of about 2 km/20 km = 10% of experiencing an instantaneous DLA-estimated rain rate exceeding 200 mm h^{-1}. Measurements from either significantly more dense rain gauges or alternatively from advantageously sited mobile/transportable rain gauges would be required to verify the large DLA-estimated instantaneous surface rain rates in the localized storm core (e.g., Smith et al. 2001).

4. Conclusions

The present study demonstrates a new buoyancy retrieval method, termed diabatic Lagrangian analysis (DLA) by deriving the potential temperature, water vapor mixing ratio, and cloud water fields in the 9 June 2009 supercell storm that was observed with multiple ground-based radars during VORTEX2. The DLA diagnoses the rain and graupel fields in the 9 June storm and evaluates Lagrangian-frame microphysical processes and the predicted variables along the field of trajectories in the evolving storm with application of the diagnosed precipitation fields. The trajectories are initialized in the storm's environment based on ambient conditions prescribed by a simple parametric representation

of temperature, water vapor mixing ratio, and pressure. The parametric environmental model is deduced from a single environmental sounding and a bilinearly varying surface temperature field estimated from the SPC operational surface mesoanalysis. Simple damping and surface flux terms are also included in the predictive Lagrangian calculations. The demonstrated ability of the DLA to generate complete, internally consistent four-dimensional (4D) buoyancy, cloud, and precipitation fields in the 9 June supercell promises to help improve the understanding of storm structure and processes in future studies of the 9 June supercell and other radar-observed storms.

A potential limitation of the present version of the DLA is its reliance on a single-moment formulation of the rain drop and graupel particle size distributions and the omission of additional hydrometeor categories. For example, the maximum expected hail size (MEHS) product from NSSL's National Mosaic and Multi-Sensor Quantitative Precipitation Estimation (QPE; NMQ) system (Zhang et al. 2011) and storm reports suggest that the 9 June storm probably contained some large hail. Thus, a key objective of future research is to develop and apply techniques to increase the number of precipitation particle categories and their independently varying size distribution parameters by incorporating polarimetric radar variables into the DLA's diagnostic precipitation algorithm. For example, work is in progress to derive rain drop mean-volume diameter, total concentration, and mixing ratio values that are simultaneously constrained by Z_H and Z_{DR} [thus expanding the parameterized rain drop distribution from a one-moment to a two-moment function as in, e.g., Zhang et al. (2001)]. Nevertheless, a broad—though promising—level of agreement has been demonstrated between the DLA-derived instantaneous surface rain rates and limited independent surface rainfall measurements in the 9 June storm case. Since the DLA is independent of vertical velocity at ground level, surface rain and graupel contents and surface rain rate could be rather straightforwardly diagnosed from WSR-88D or other operational radar reflectivity volumes or composite fields. Related goals for future studies are to compare analyses generated by the DLA with corresponding analyses using the ensemble Kalman filter (e.g., Dowell et al. 2004; Marquis et al. 2012; Dawson et al. 2012) and the three-dimensional variational data assimilation (3DVAR) method (e.g., Gao and Stensrud 2012) and to explore possible hybrid analysis approaches.

The processes involved in cold pool formation and the subsequent impact of cold pools on storm dynamics could be studied in greater detail using the DLA method. For example, Betts (1984) reports an "evaporation line" saturation point structure that implies the concerted action of mixing and rain evaporation in storm outflow, noting that the (elusive) "source of . . . low-θ_e downdraft air is of importance" and also "needs further kinematic and dynamic study using the Doppler radar data" (p. 2206). The classical process of low-level mesocyclone development via the solenoidal generation of horizontal vorticity combined with tilting and intense stretching at the main updraft base (e.g., Klemp and Rotunno 1983; Rotunno and Klemp 1985) can also be studied using the Lagrangian-analyzed fields of θ_v and hydrometeor loading buoyancy in the baroclinic forward- and rear-flank updraft inflow regions of observed storms. With its emphasis on thermodynamic, microphysical, and transportive processes acting along individual trajectories, the DLA offers a computationally efficient and potentially useful tool to help advance studies of precipitation downdraft processes, cold pool formation, and the origins of low-level rotation in supercells.

Acknowledgments. The author gratefully acknowledges the helpful discussions with Ted Mansell and Lou Wicker concerning the Lagrangian model's microphysical parameterizations, which follow NSSL's COMMAS model. Ted Mansell is also gratefully acknowledged for providing output of his high-resolution Geary storm simulation and offering his asymptotic formulation for the mean rain fall speed that was used to calculate surface rain rates from the DLA output. James Correia (SPC) provided SPC mesoanalysis output products that were assimilated into the parametric storm-environment model. Dennis Flanigan (formerly of NCAR-EOL) developed FORAY (a predecessor of the present RADX radar translator developed by NCAR-EOL) concurrently with the present study to translate WSR-88D super-resolution KDDC radar volumes to DORADE format in collaboration with Eddie Forren (NSSL) and the author, who served as a FORAY beta tester. Insightful formal editorial review comments provided by Adam Houston, Erik Rasmussen, and Matt Kumjian led to significant improvements of the revised manuscript. Paul Markowski and Yvette Richardson led the mobile mesonet data collections, and Chris Weiss led the StickNet data collections during VORTEX2. The author is also grateful to the many scientists who have contributed to the collection, archival, and dissemination, and subsequent analyses of the VORTEX2 dataset. Support for the current project was provided under National Science Foundation Grants AGS-0130316, AGS-0638572, and AGS-0802717, and the National Severe Storms Laboratory Director's Discretionary Fund.

REFERENCES

Atlas, D., R. C. Srivastava, and R. S. Sekhon, 1973: Doppler radar characteristics of precipitation at vertical incidence. *Rev. Geophys.,* **11,** 1–35.

Betts, A. K., 1984: Boundary layer thermodynamics of a high plains severe storm. *Mon. Wea. Rev.,* **112,** 2199–2211.

Biggerstaff, M., and Coauthors, 2005: The Shared Mobile Atmospheric Research and Teaching Radar: A collaboration to enhance research and teaching. *Bull. Amer. Meteor. Soc.,* **86,** 1263–1274.

Brandes, E. A., 1984: Relationships between radar-derived thermodynamic variables and tornadogenesis. *Mon. Wea. Rev.,* **112,** 1033–1052.

Burgess, D. W., E. R. Mansell, C. M. Schwarz, and B. J. Allen, 2010: Tornado and tornadogenesis events seen by the NOXP, X-band, dual-polarization radar during VORTEX2 2010. Preprints, *25th Conf. on Severe Local Storms,* Denver, CO, Amer. Meteor. Soc., 5.2. [Available online at https://ams.confex.com/ams/25SLS/techprogram/paper_176164.htm.]

Dawson, D. T., II, L. J. Wicker, E. R. Mansell, and R. L. Tanamachi, 2012: Impact of the environmental low-level wind profile on ensemble forecasts of the 4 May 2007 Greensburg, Kansas, tornadic storm and associated mesocyclones. *Mon. Wea. Rev.,* **140,** 696–716.

Doswell, C. A., III, H. E. Brooks, and R. A. Maddox, 1996: Flash flood forecasting: An ingredients-based methodology. *Wea. Forecasting,* **11,** 560–581.

Doviak, R. J., and D. S. Zrnic, 1984: *Doppler Radar and Weather Observations.* Academic Press, 458 pp.

Dowell, D. C., F. Zhang, L. J. Wicker, C. Snyder, and N. A. Crook, 2004: Wind and temperature retrievals in the 17 May 1981 Arcadia, Oklahoma, supercell: Ensemble Kalman filter experiments. *Mon. Wea. Rev.,* **132,** 1982–2005.

Gao, J., and D. J. Stensrud, 2012: Assimilation of reflectivity data in a convective-scale, cycled 3DVAR framework with hydrometeor classification. *J. Atmos. Sci.,* **69,** 1054–1065.

Gunn, R., and G. D. Kinzer, 1949: The terminal velocity of fall for water droplets in stagnant air. *J. Meteor.,* **6,** 243–248.

Hane, C., C. Ziegler, and P. Ray, 1988: Use of velocity fields from Doppler radars to retrieve other variables in thunderstorms. *Instruments and Techniques for Thunderstorm Observation and Analysis,* E. Kessler, Ed., Vol. 3, *Thunderstorms: A Social, Scientific, and Technological Documentary,* 215–234.

Hauser, D., and P. Amayenc, 1986: Retrieval of cloud water and water vapor contents from Doppler radar data in a tropical squall line. *J. Atmos. Sci.,* **43,** 823–838.

Kessinger, C., P. Ray, and C. Hane, 1987: The Oklahoma squall line of 19 May 1977. Part I: A multiple Doppler analysis of convective and stratiform structure. *J. Atmos. Sci.,* **44,** 2840–2864.

Klemp, J. B., 1987: Dynamics of tornadic thunderstorms. *Annu. Rev. Fluid Mech.,* **19,** 369–402.

——, and R. Rotunno, 1983: A study of the tornadic region within a supercell thunderstorm. *J. Atmos. Sci.,* **40,** 359–377.

Kumjian, M. R., and A. V. Ryzhkov, 2012: The impact of size sorting on the polarimetric radar variables. *J. Atmos. Sci.,* **69,** 2042–2060.

MacGorman, D. R., and Coauthors, 2008: TELEX: The Thunderstorm and Electrification Lightning Experiment. *Bull. Amer. Meteor. Soc.,* **89,** 997–1013.

Majcen, M., P. Markowski, Y. Richardson, D. Dowell, and J. Wurman, 2008: Multipass objective analysis of Doppler radar data. *J. Atmos. Oceanic Technol.,* **25,** 1845–1858.

Mansell, E. R., and C. L. Ziegler, 2013: Aerosol effects on simulated storm electrification and precipitation in a two-moment bulk microphysics model. *J. Atmos. Sci.,* **70,** 2032–2050.

——, ——, and E. Bruning, 2010: Simulated electrification of a small thunderstorm with two-moment bulk microphysics. *J. Atmos. Sci.,* **67,** 171–194.

Marquis, J., Y. Richardson, P. Markowski, D. Dowell, and J. Wurman, 2012: Tornado maintenance investigated with high-resolution dual-Doppler and EnKF analysis. *Mon. Wea. Rev.,* **140,** 3–27.

May, R. M., M. I. Biggerstaff, and M. Xue, 2007: A Doppler radar emulator with an application to the detectability of tornadic signatures. *J. Atmos. Oceanic Technol.,* **24,** 1973–1996.

McGinley, J., 1982: A diagnosis of alpine lee cyclogenesis. *Mon. Wea. Rev.,* **110,** 1271–1287.

Oye, R., C. Mueller, and S. Smith, 1995: Software for radar translation, visualization, editing, and interpolation. Preprints, *27th Conf. on Radar Meteorology,* Vail, CO, Amer. Meteor. Soc., 359–361.

Pauley, P., and X. Wu, 1990: The theoretical, discrete, and actual response of the Barnes objective analysis scheme for one- and two-dimensional fields. *Mon. Wea. Rev.,* **118,** 1145–1163.

Ray, P. S., and K. L. Sangren, 1983: Multiple-Doppler radar network design. *J. Climate Appl. Meteor.,* **22,** 1444–1454.

——, K. K. Wagner, K. W. Johnson, J. J. Stephens, W. C. Bumgarner, and E. A. Mueller, 1978: Triple-Doppler observations of a convective storm. *J. Appl. Meteor.,* **17,** 1201–1212.

——, M. Gilet, and K. W. Johnson, 1980a: Part IV: Motion field synthesis and radar placement. *Bull. Amer. Meteor. Soc.,* **61,** 1184–1189.

——, C. L. Ziegler, W. L. Bumgarner, and R. J. Serafin, 1980b: Single- and multiple-Doppler radar observations of tornadic storms. *Mon. Wea. Rev.,* **108,** 1607–1625.

Rotunno, R., and J. Klemp, 1985: On the rotation and propagation of simulated supercell thunderstorms. *J. Atmos. Sci.,* **42,** 271–292.

Schwarz, C. M., and D. W. Burgess, 2010: Verification of the Origins of Rotation in Tornadoes Experiment, part 2 (VORTEX2): Data from the NOAA (NSSL) X-band dual-polarized radar. Preprints, *25th Conf. on Severe Local Storms,* Denver, CO, Amer. Meteor. Soc., P6.1.

Shapiro, A., K. M. Willingham, and C. K. Potvin, 2010: Spatially variable advection correction of radar data. Part I: Theoretical considerations. *J. Atmos. Sci.,* **67,** 3445–3456.

Skinner, P. S., C. C. Weiss, J. L. Schroeder, L. J. Wicker, and M. I. Biggerstaff, 2011: Observations of the surface boundary structure within the 23 May 2007, Perryton, Texas supercell. *Mon. Wea. Rev.,* **139,** 3730–3749.

Smith, J. A., M. L. Baeck, Y. Zhang, and C. A. Doswell III, 2001: Extreme rainfall and flooding from supercell thunderstorms. *J. Hydrometeor.,* **2,** 469–489.

Straka, J. M., E. N. Rasmussen, and S. E. Fredrickson, 1996: A mobile mesonet for finescale meteorological observations. *J. Atmos. Oceanic Technol.,* **13,** 921–936.

Testud, J., E. LeBouar, E. Obligis, and M. Ali-Mehenni, 2000: The rain profiling algorithm applied to polarimetric weather radar. *J. Atmos. Oceanic Technol.,* **17,** 332–356.

Vasiloff, S., 2012: Evaluation of dual-polarization QPE: Initial results for spring and summer 2012: Final report, MOU Task1.1, NOAA/NSSL, 48 pp.

Waugh, S., and S. E. Fredrickson, 2010: An improved aspirated temperature system for mobile meteorological observations, especially in severe weather. Preprints, *25th Conf. on Severe*

Local Storms, Denver, CO, Amer. Meteor. Soc., P5.2. [Available online at https://ams.confex.com/ams/25SLS/techprogram/paper_176205.htm.]

Weiss, C. C., and J. L. Schroeder, 2008: The 2007 and 2008 MOBILE Experiment: Development and testing of the TTU StickNet platforms. Preprints, *24th Conf. on Severe Local Storms,* Savannah, GA, Amer. Meteor. Soc., 5.1. [Available online at https://ams.confex.com/ams/24SLS/techprogram/paper_141842.htm.]

Wood, V. T., and R. A. Brown, 1997: Effects of radar sampling on single-Doppler velocity signatures of mesocyclones and tornadoes. *Wea. Forecasting,* **12,** 928–938.

Wurman, J., 2001: The DOW mobile multiple-Doppler network. Preprints, *30th Int. Conf. on Radar Meteorology,* Munich, Germany, Amer. Meteor. Soc., P3.3. [Available online at https://ams.confex.com/ams/30radar/techprogram/paper_21572.htm.]

——, and S. Gill, 2000: Finescale radar observations of the Dimmitt, Texas (2 June 1995), tornado. *Mon. Wea. Rev.,* **128,** 2135–2164.

——, J. Straka, E. Rasmussen, M. Randall, and A. Zahrai, 1997: Design and deployment of a portable, pencil-beam, pulsed, 3-cm Doppler radar. *J. Atmos. Oceanic Technol.,* **14,** 1502–1512.

——, D. Dowell, Y. Richardson, P. Markowski, E. Rasmussen, D. Burgess, L. Wicker, and H. Bluestein, 2012: The Second Verification of the Origins of Rotation in Tornadoes Experiment (VORTEX2). *Bull. Amer. Meteor. Soc.,* **93,** 1147–1170.

Zhang, G., J. Vivekanandan, and E. A. Brandes, 2001: A method for estimating rain rate and drop size distribution from polarimetric radar measurements. *IEEE Trans. Geosci. Remote Sens.,* **39,** 830–841.

Zhang, Z., and Coauthors, 2011: National Mosaic and Multi-Sensor QPE (NMQ) System. *Bull. Amer. Meteor. Soc.,* **92,** 1321–1338.

Ziegler, C. L., 1985: Retrieval of thermal and microphysical variables in observed convective storms. Part I: Model development and preliminary testing. *J. Atmos. Sci.,* **42,** 1487–1509.

——, 2013: A diabatic Lagrangian technique for the analysis of convective storms. Part I: Description and validation via an observing system simulation experiment. *J. Atmos. Oceanic Technol.,* **30,** 2248–2265.

——, P. S. Ray, and N. C. Knight, 1983: Hail growth in an Oklahoma multicell storm. *J. Atmos. Sci.,* **40,** 1768–1791.

——, D. Kennedy, and E. N. Rasmussen, 2004: A wireless network for collection and synthesis of mobile mesoscale weather observations. *J. Atmos. Oceanic Technol.,* **21,** 1659–1669.

——, E. Mansell, J. Straka, D. MacGorman, and D. Burgess, 2010: The impact of spatial variations of low-level stability on the life cycle of a simulated supercell storm. *Mon. Wea. Rev.,* **138,** 1738–1766.